Coexisting and cooperating light–matter interaction regimes in a polaritonic photovoltaic system

OPEN ACCESS
IOP Publishing
Journal of Optics
J. Opt. **25** (2023) 105401 (10pp)
https://doi.org/10.1088/2040-8986/acf2ac

Coexisting and cooperating light–matter interaction regimes in a polaritonic photovoltaic system

V Caligiuri[1,2,7,*], S Siprova[1,2,7], A Patra[1,3], G E Lio[4,5], R Termine[2,6,*], S Cilurzo[1], A Golemme[1,2,6] and A De Luca[1,2,*]

[1] Department of Physics, University of Calabria, via P. Bucci, 31C, 87036 Rende, CS, Italy
[2] CNR Nanotec UOS Rende, via P. Bucci, 31D, 87036 Rende, CS, Italy
[3] Istituto Italiano di Tecnologia, via Morego 30, 16163 Genova, GE, Italy
[4] Physics Department, and European Laboratory for Non-Linear Spectroscopy (LENS) at University of Florence, Via Nello Carrara 1, 50019, Sesto Fiorentino, Florence, Italy
[5] Consiglio Nazionale delle Ricerche—National Institute of Optics, CNR-INO, 50019 Sesto Fiorentino, FI, Italy
[6] LASCAMM-CR, Unità INSTM della Calabria, via P. Bucci, 14C, 87036 Rende, CS, Italy

E-mail: vincenzo.caligiuri@unical.it, roberto.termine@cnr.it and antonio.deluca@unical.it

Received 21 April 2023, revised 28 July 2023
Accepted for publication 22 August 2023
Published 1 September 2023

Abstract

Common quantum frameworks of light–matter coupling demonstrate the interaction between an atom and a cavity occurring through a single feedback channel: an exciton relaxes by emitting a photon that is stored in the cavity for several roundtrips before being re-absorbed to create another exciton, and so on. However, the possibility for the excited system to relax through two different channels belonging to two different regimes has been, until now, neglected. Here, we investigate the case in which the strong coupling regime and the photovoltaic effect cooperate to enhance the wavelength-dependent photocurrent conversion efficiency (defined as the incident photons to converted electrons ratio, namely the external quantum efficiency—EQE) of a photovoltaic cell specifically engineered to behave as an optical cavity tuned to the excitonic transition of the embedded active material ($CH_3NH_3PbI_3$ perovskite). We exploit the angular dispersion of such photovoltaic cell to show that when the cavity mode approaches the energy of the exciton, the strong coupling regime is achieved and the EQE is significantly enhanced with respect to a classic configuration serving as a benchmark. Our findings do not aim at demonstrating an immediate impact in enhancing the performance of photovoltaic systems but, rather, constitute a proof-of-principle experimental demonstration of how the photovoltaic effect can benefit from the generation of polaritons. Nonetheless, such a peculiar cooperating dual-light–matter interaction could be exploited in future polaritonic photovoltaic architectures.

[7] These authors contributed equally.
[*] Authors to whom any correspondence should be addressed.

Supplementary material for this article is available online

Keywords: strong coupling, polaritonic photovoltaics, photovoltaics, meta-voltaics, perovskite, metal/insulator/metal cavities

(Some figures may appear in colour only in the online journal)

1. Introduction

The interaction between excitons and the electromagnetic environment in their proximity can be weak or strong [1, 2]. In the so-called 'strong coupling regime', a new quasiparticle called 'polariton' is generated whose nature shares features of both light and matter [3–7]. The insurgence of polaritons can substantially improve the performances of charge-transport related phenomena [8, 9]. When a nanometrically delocalized exciton strongly couples with a macroscopically delocalized cavity mode photon, a polariton arises whose mixed-nature wavefunction results coherently delocalized on the length scale of the size of the cavity [10]. Feist and Garcia-Vidal demonstrated that exciton polaritons manifest much longer diffusion lengths than excitons [11]. DelPo *et al* demonstrated that charge transfer from polaritons can be so fast to compete with the polariton relaxation time, experimentally justifying the use of polaritons for charge-transfer-related applications [12], while Wang *et al* demonstrated that the rate of polariton-based energy transfer processes is largely increased with respect to the case of simple excitons [13]. In 2022, Zeb *et al* demonstrated that the so-called incoherent charge hopping process rates occurring in organic materials where Frenkel excitons are mostly present can be largely improved by the presence of polaritons [14]. The same year, leveraging on the aforementioned strongly delocalized character of polaritons, Liu *et al* proposed the introduction of a polariton-based 'antenna complex' in a system that mimics the natural photosynthesis processes for charge transfer [15]. On a theoretical side, the case for perovskites, where mostly Wannier excitons are expected to be present, is not clear yet but some recent works suggested that even in semiconductors a similar beneficial effect can be obtained. For example, Chevry *et al* demonstrated that external electric fields could accelerate polaritons by forming new quasiparticles termed polaron-polaritons [16]. It has also been shown that the transport phenomena associated to excitons can be substantially improved by the occurrence of polaritons since, in this last framework, transport is sustained by delocalized polariton modes rather than by tunneling processes [17]. Exceptional propagation lengths of hundreds of microns were demonstrated for polaritons generated in an organic material through the hybridization of Bloch waves and excitons [18].

It seems thus reasonable to expect that photovoltaics could largely benefit from the adoption of a polaritonic environment. For example, it has been recently shown that in photovoltaic systems based on organic polaritons, losses can be substantially lower than in classic exciton-based organic photovoltaic cells [19].

In this paper, we showcase a 'Metal–Insulator–Metal photovoltaic cell' (MIM-cell), that is a system in which strong coupling regime and photovoltaic effect coexist and cooperate to enhance the external quantum efficiency (EQE) of a perovskite-based photovoltaic cell. In the proposed system, the photovoltaic effect involves polaritons, leading to a twofold enhancement of EQE. A possible explanation of the beneficial mechanism lying at the basis of the EQE enhancement due to polaritons could be searched in the enhanced coherent delocalization of the polaritons with respect to excitons. As reported by Schachenmayer *et al* such a feature shifts the charge transfer from tunneling-based channels, typical of strongly localized excitons, to largely delocalized polaritonic modes that are far less sensitive to defects and associated non-radiative relaxation channels [17]. Our data are far from depicting a technologically mature scenario, but they reveal that this light–matter interaction occurring through the unconventional path of two cooperating regimes coexisting within the same system can be observed also using perovskites.

2. Results and discussion

The architecture of the MIM-cell is made of a photovoltaic cell embedded within a resonator consisting of a metal/insulator/-metal (MIM) cavity. Here we lend the suffix 'meta' and use it with slightly loose hand, to underline that the simple addition of a metallic layer to a classic photovoltaic architecture leads to a resonant response with remarkably different photovoltaic properties. As shown in figure 1, the MIM-cell is fabricated over a glass substrate by depositing different layers.

The proposed MIM-cell was fabricated by stacking from the bottom to the top: Au/ITO/PEDOT:PSS/$CH_3NH_3PbI_3$ perovskite/$PC_{61}BM$/Bathocuproine/Ag. Here, Au and Ag play the role of both the metallic mirrors of the resonator and the photovoltaic cell electrodes. The perovskite represents the active medium that, together with all the other dielectric transport layers, constitutes also the compound dielectric core of the MIM cavity. As such, the MIM-cell is endowed with an angular dispersion stemming from its MIM configuration so that, upon moving the angle of incidence of light radiation away from normal incidence, the wavelength of the cavity mode blue-shifts. Here, it is important to underline that the presence of a top Ag layer, which is usually supposed to be both highly reflective and dissipative, does not prevent the excitation of cavity modes. The peculiar complex refractive index of Ag, indeed, makes it a so-called Hermitian metal, meaning that the imaginary part of its refractive index is far larger than the real one. As a result, photons with frequency within the

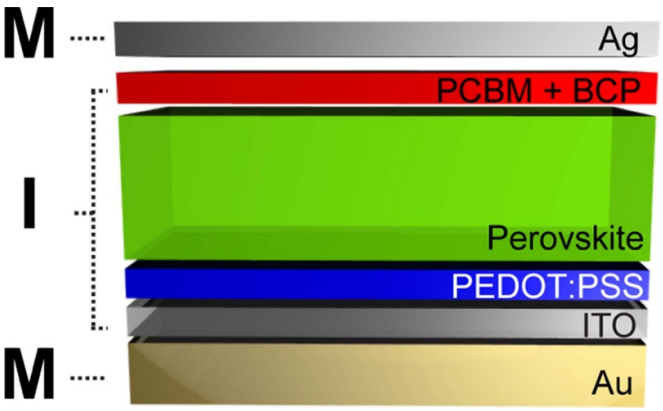

Figure 1. Sketch of the MIM-cell consisting in a perovskite-based photovoltaic cell embedded between two external metallic mirrors that constitute, at the same time, the two reflectors of a metal/insulator/metal resonator and the electrodes of the photovoltaic cell. The different layers constituting the device are, starting from the bottom: the gold electrode; indium doped tin oxide (ITO), poly(3,4-ethylenedioxythiophene) polystyrene sulfonate (PEDOT:PSS); $CH_3NH_3PbI_3$ perovskite; phenyl-C_{61}-butyric-acid-methyl-ester (PCBM); bathocuproine (BCP); the silver electrode.

visible range can tunnel through the Ag layer under the shape of a mostly purely evanescent wave that is not and should not be confused with a surface plasmon [20].

To optimize the photocurrent performances of a photovoltaic system, thick gain material layers are commonly used [21]. In this case, however, due to the high optical density of the perovskite and to its continuous absorption band, it is very difficult to observe the signatures of the strong coupling regime, like mode anti-crossing and Rabi splitting (2 Ω), in scattering parameters like transmittance, absorbance and reflectance [22]. Such features result far more visible if a thin layer of perovskite is used instead of a thick one. Therefore, with the aim of demonstrating the capability of the architecture in figure 1 to sustain strong coupling and polaritons, we carried out scattering matrix method (SMM) simulations by considering a 40 nm thick perovskite layer, thinner than the one we experimentally use. To tune the resonance of the MIM-cell to the wavelength of the exciton, the thickness of the ITO layer is fixed to 250 nm. The simulated structure, made of Ag (20 nm)/PCBM + BCP (50 nm in total), $CH_3NH_3PbI_3$ (40 nm), PEDOT:PSS (50 nm), ITO (250 nm), Au (100 nm) is sketched in figure 2(a). We highlight that the thickness of both the perovskite and the ITO layer used for the simulation are different from the experimental ones. Figures 2(b) and (c) show the simulated absorbance (1 – Reflectance − Transmittance) maps of such MIM-cell for p- and s-polarization, respectively, as a function of light incidence angle θ (defined in terms of its deviation from normal incidence). The refractive index of all the involved materials was experimentally measured through spectroscopic ellipsometry (see supporting information). Such an investigation revealed two excitonic transitions, highlighted with dashed white lines in figures 2(b) and (c) and labeled as 'HE-Exciton' and 'LE-Exciton' in figure 2(c). By increasing the incidence angle, the unperturbed cavity mode, occurring for both polarizations at about 830 nm, blue shifts approaching the LE-Exciton wavelength. Such a behavior is expected for a MIM cavity, that follows the well-known Fabry–Pérot angular dispersion $\lambda(\theta_i) = \lambda_0\sqrt{1-\left(\sin^2(\theta_i)/n_{eff}^2\right)}$. Here, θ_i is the angle of incidence, while considering that the refractive index of both the perovskite and the ITO layers are far larger than those of PEDOT:PSS or PCBM + BCP, the quantity n_{eff} can be simply calculated as the thickness weighted average refractive index between ITO and perovskite, $n_{eff} = (n_{ITO}\cdot t_{ITO} + n_{PSK}\cdot t_{PSK})/2$. The quantity t_D is the total thickness of the dielectric layer inside the cell, calculated by summing all the thicknesses reported in figure 2(a), so that $t_D = 390$ nm. The quantity λ_0 is the resonant wavelength of the cavity at normal incidence, that can be calculated by leveraging on the analogy between quantum mechanics and classic electromagnetism and, in particular, on the isomorphism between the Helmholtz and Schrödinger equations [20]. For our MIM-cell, the quantity λ_0, as well as all the additional even harmonics can be calculated by geometrically resolving the following equation: $\tan(2\pi/\lambda\cdot n_{eff}\cdot t_D/2) = \kappa_M/n_{eff}$, where κ_M is the imaginary part of the refractive index of Ag. By including all these parameters, the geometric resolution of the previous relation found as the wavelengths where the crossing between the left and the right part of the equation occurs, are $\lambda_{1\text{-even}} = 840$ nm, $\lambda_{2\text{-even}} = \sim 600$ nm and $\lambda_{3\text{-even}} = \sim 470$ nm. These modes correspond to the first three even harmonics sustained by the MIM-cell. The odd harmonics can be calculated through the related formula—$\cot(2\pi/\lambda\cdot n_{eff}\cdot t_D/2) = \kappa_M/n_{eff}$ that provides as solutions $\lambda_{1\text{-odd}} = \sim 690$ nm and $\lambda_{2\text{-odd}} = \sim 530$ nm, that correspond to the first two odd harmonics sustained by the cavity. Despite these are approximated wavelengths, such an analysis clarifies the nature of the involved cavity resonances and highlights the presence of additional harmonics lying within the interband transition absorbance region of the perovskite.

A first qualitative investigation of the absorbance maps shown in figures 2(b) and (c) reveals a significant deviation of the absorbance maxima from the original energy of both the two excitonic transitions (LE and HE), evidencing a strong perturbation of the pristine system. We associate this behavior to the occurrence of strong coupling. Since two excitons and one cavity mode are involved, the coupling dynamics is that of three strongly coupled oscillators, with the consequent generation of a low-energy polariton (LP), a middle-energy polariton (MP) and a high-energy polariton (HP). The spectral dispersion for all these three polaritonic branches follows the trend indicated by the colored dots (blue, green and red dots referred to HP, MP and LP, respectively) in figures 2(b) and (c), for both p- and s-polarizations.

To gain insight on the nature of the detected polariton we calculated the Hopfield coefficients for each of them [23–28]. Results are shown in figures 2(d) and (e) for the P- and S-polarization, respectively. For both polarizations very similar

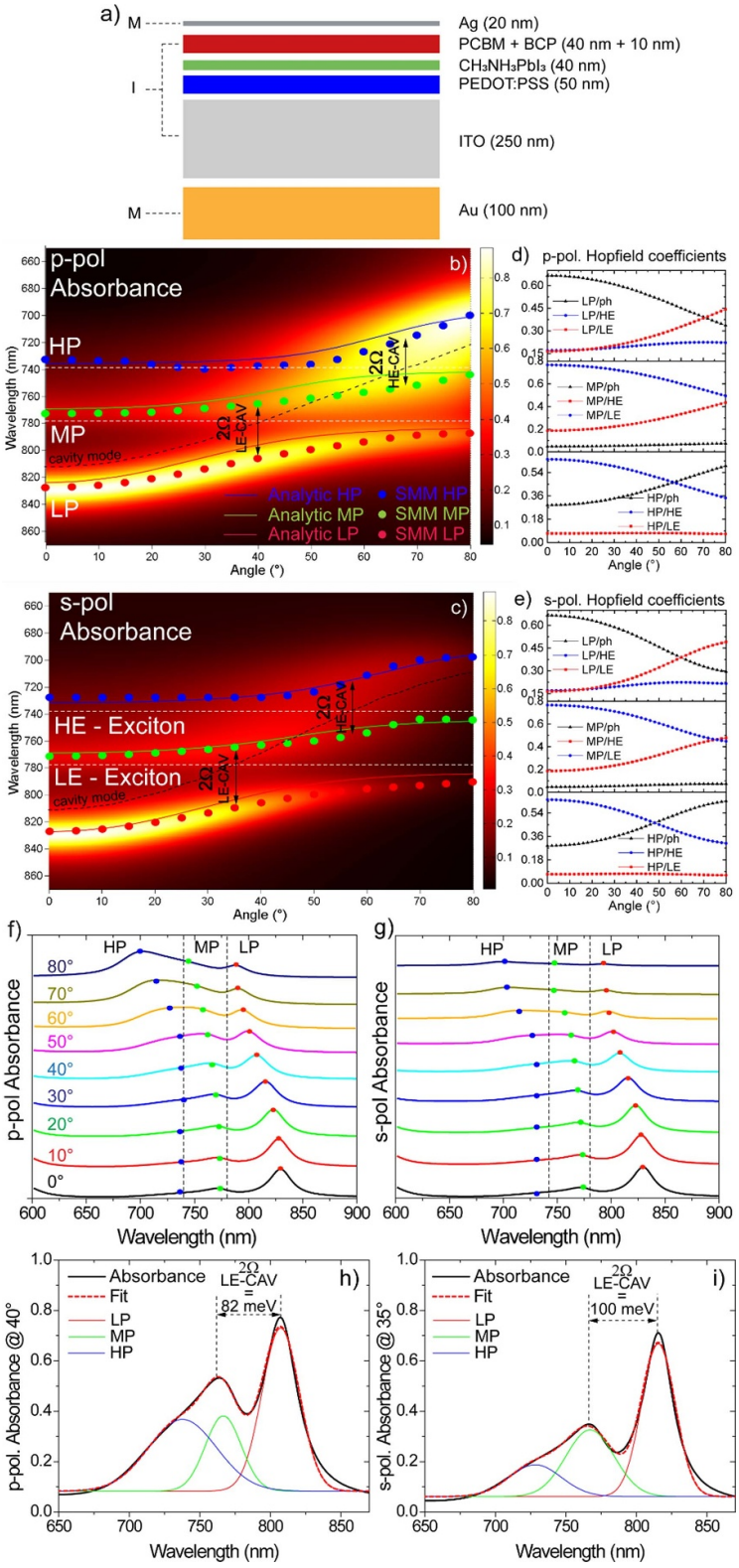

Figure 2. (a) Sketch of the simulated structure. (b) P- and (c) s-polarization absorbance ($1 - R - T$) maps as a function of light incidence angle θ calculated via SMM simulations for a 40 nm perovskite and 250 nm ITO MIM-Cell. The overlapped blue, green and red dots represent the central wavelengths λ_0 of the Gaussian oscillators used to fit the absorbance curves through equation (1) for the HP, MP and LP. The blue, green and red solid lines, instead, represent the eigenvalues of the interaction Hamiltonian of equation (2). Dashed white lines represent the two excitonic transitions of $CH_3NH_3PbI_3$ perovskite. (d) P- and (f) S-polarization Hopfield coefficients calculated for each polariton. (f) P- and (g) S-polarization absorbance spectra extrapolated from (b) and (c) at ten different incident angles, stacked on top of each other for clarity. Also in this case the colored dots representing λ_0 from equation (2) have been overlapped with the bare absorbance curves. (h) P-polarization and (i) S-polarization absorbance curves extrapolated from (b) at $\theta = 40^\circ$ and from (c) at $\theta = 35^\circ$, to evaluate a Rabi splitting of about 82 meV for p-pol. and 100 meV for s-pol.

considerations can be drawn: at small angles, the LP holds mostly a photonic nature and gradually increases its mixing with LE with the angle. On the contrary, the HP holds mainly and excitonic character at small angles and gradually acquires a photonic flavor while increasing the angle of incidence. The MP, in the end, holds mainly an excitonic character and, therefore results lossy and less visible than the others.

To better identify the occurrence of the strong coupling regime in the simulated thin-perovskite system, we fitted the absorbance curves at ten relevant angles (from 0° to 80° with 10° steps) with a tri-Gaussian function:

$$A_{\mathrm{f}}(\lambda) = \sum_{i=1}^{3} A_{0_i} \mathrm{e}^{\left(\frac{(\lambda-\lambda_{0_i})}{\sigma_i}\right)^2}. \qquad (1)$$

Here, A_0, λ_0 and σ are the amplitude, central wavelength and standard deviation of the *i*th oscillator, respectively. To each Gaussian oscillator, a specific mode is associated. In particular, the longer-, middle- and shorter-wavelength oscillator can be related to the low-, middle- and high-energy polaritonic branch labeled as 'LP', 'MP' and 'HP', respectively. The central wavelengths λ_0 calculated through equation (1) can be readily overlapped to both the absorbance maps (see figures 2(b) and (c)) and to the extrapolated absorbance curves, as shown in figures 2(b) and (e). The resulting graph allows to precisely follow the dispersion of the three relevant quantities, HP, MP and LP.

To confirm the achievement of the strong coupling, we analytically modeled the entire system through the interaction Hamiltonian reported in equation (2):

$$H = \begin{bmatrix} E_{\mathrm{CAV}} & g_{\mathrm{LE-CAV}} & g_{\mathrm{HE-CAV}} \\ g_{\mathrm{LE-CAV}} & E_{\mathrm{LE}} & g_{\mathrm{LE-HE}} \\ g_{\mathrm{HE-CAV}} & g_{\mathrm{LE-HE}} & E_{\mathrm{HE}} \end{bmatrix}. \qquad (2)$$

Here E_{CAV}, E_{LE} and E_{HE} are the energies of the cavity mode, of the LE- and of the HE-Exciton. The terms $g_{\mathrm{HE-CAV}} = \Omega_{\mathrm{HE-CAV}}$, $g_{\mathrm{LE-CAV}} = \Omega_{\mathrm{LE-CAV}}$ and $g_{\mathrm{HE-LE}}$ are the cavity/HE-Exciton, cavity/LE-Exciton and HE-Exciton/LE-Exciton coupling terms, respectively. Since there is no interaction between the excitons, in our case the term $g_{\mathrm{HE-LE}}$ is equal to 0.

The occurrence of the strong coupling between the low-energy excitonic transition and the cavity mode was evaluated by examining the absorbance curves at the anti-crossing angles $\theta = 40°$ for the p-polarization (figure 2(f)) and $\theta = 35°$ for the s-polarization (figure 2(g)). The unperturbed cavity dispersion (dashed black line in figures 2(b) and (c)) has been numerically calculated (see supporting information). For both cases, the Rabi Splitting was calculated by deconvoluting the absorbance curves with three Gaussian curves representing the LP, MP and the HP (see figures 2(f) and (g)). Hereafter, we report only the relevant cases of the coupling between the cavity mode and the LE-Exciton. For the p-polarization case, a Rabi Splitting $2\,\Omega_{\mathrm{LE-CAV}} = 82$ meV was calculated (see figure 2(f)) while, for the s-polarization, $2\,\Omega_{\mathrm{LE-CAV}} = 100$ meV. To assess the occurrence of the strong coupling, the quantity $2\,\Omega_{\mathrm{LE-CAV}}$ was compared to the linewidth of the cavity mode and of the excitonic transition of the perovskite. In this case, they are equal to $\Delta E_{\mathrm{CAV}} = 41$ meV and $\Delta E_{\mathrm{EXC}} \sim 40$ meV, respectively. The full width at half-maximum of the cavity mode was derived as a parameter from equation (1) for the absorbance curve at normal incidence (0°), far from the anti-crossing point. At $\theta = 0°$, indeed, the energy of the LP mode is very far from that of the excitonic transition, ensuring that, at this angle, the mode still holds a marked 'cavity' character, a consideration that is also confirmed by the Hopfield coefficient shown in figure 2(d). The exciton linewidth, on the other hand, was calculated directly from the ellipsometrical measurements (imaginary part of the refractive index of a deposited 40 nm perovskite film). For the p-polarization, $\Omega_{\mathrm{LE-CAV}} \sim \Delta E_{\mathrm{CAV}} \sim \Delta E_{\mathrm{EXC}}$ so that the system is barely in the strong coupling regime. On the contrary, for the s-polarization $\Omega_{\mathrm{LE-CAV}} > \Delta E_{\mathrm{CAV}}$ and $\Omega_{\mathrm{LE-CAV}} > \Delta E_{\mathrm{EXC}}$, confirming the achievement of the strong coupling condition. In the end, we note that the nature of the polaritonic mode can affect its spectral linewidth. As a consequence, for example, at small angles the LP holds a strong cavity-like behavior (see figure 2(d)) and inherits the *Q*-factor of the cavity mode from which it is generated. On the contrary, the highly lossy excitonic features of the LP at large angles, confirmed by the increasing mixing with HE as calculated in the Hopfield coefficient of figure 2(d), broaden its linewidth.

As already mentioned, however, a thin active layer is rarely used in experimental frameworks. A thickness of the active layer close to 40 nm would be of the same order as roughness, creating pinholes and increasing shunt currents. In addition, the absorption of the active layer would be very low, inducing low photogenerated currents. Both effects would prevent performance measurements with reasonable accuracy. Nonetheless, the simulations described above can guide the interpretation of experimental results obtained using thicker perovskite layers. Therefore, MIM-cells with the architecture shown in figure 1 were fabricated, with a thickness of the perovskite layer of about 180 nm. To keep the cavity mode and the exciton in tune with each other, the thickness of the ITO layer was decreased to 25 nm. The thickness of the other layers was: Au (100 nm), PEDOT:PSS (50 nm), phenyl-C_{61}-butyric acid methyl ester (40 nm), bathocuproine (10 nm), Ag (20 nm). The thickness of the bottom layer ensures optimal conduction properties and suitable quality factor of the cavity mode, while for the top metal, a thickness equal to 20 nm is the best compromise between homogeneity, light tunneling to the active material and an efficient cavity response.

The reflectance of a typical MIM-cell of this kind, measured by an ellipsometric setup is shown in figures 3(a) and (b) as a function of the incidence angle. At $\theta = 20°$, a cavity mode around 850 nm is generated for both s- and p-polarizations. By increasing the incidence angle, the resonance blue-shifts for both polarizations. Due to the highly lossy nature of the MIM-cell and the high refractive index of the embedded perovskite, the angular dispersion observed for p-polarization does not significantly diverge from what observed in the s-polarization case, as would be expected in a standard MIM

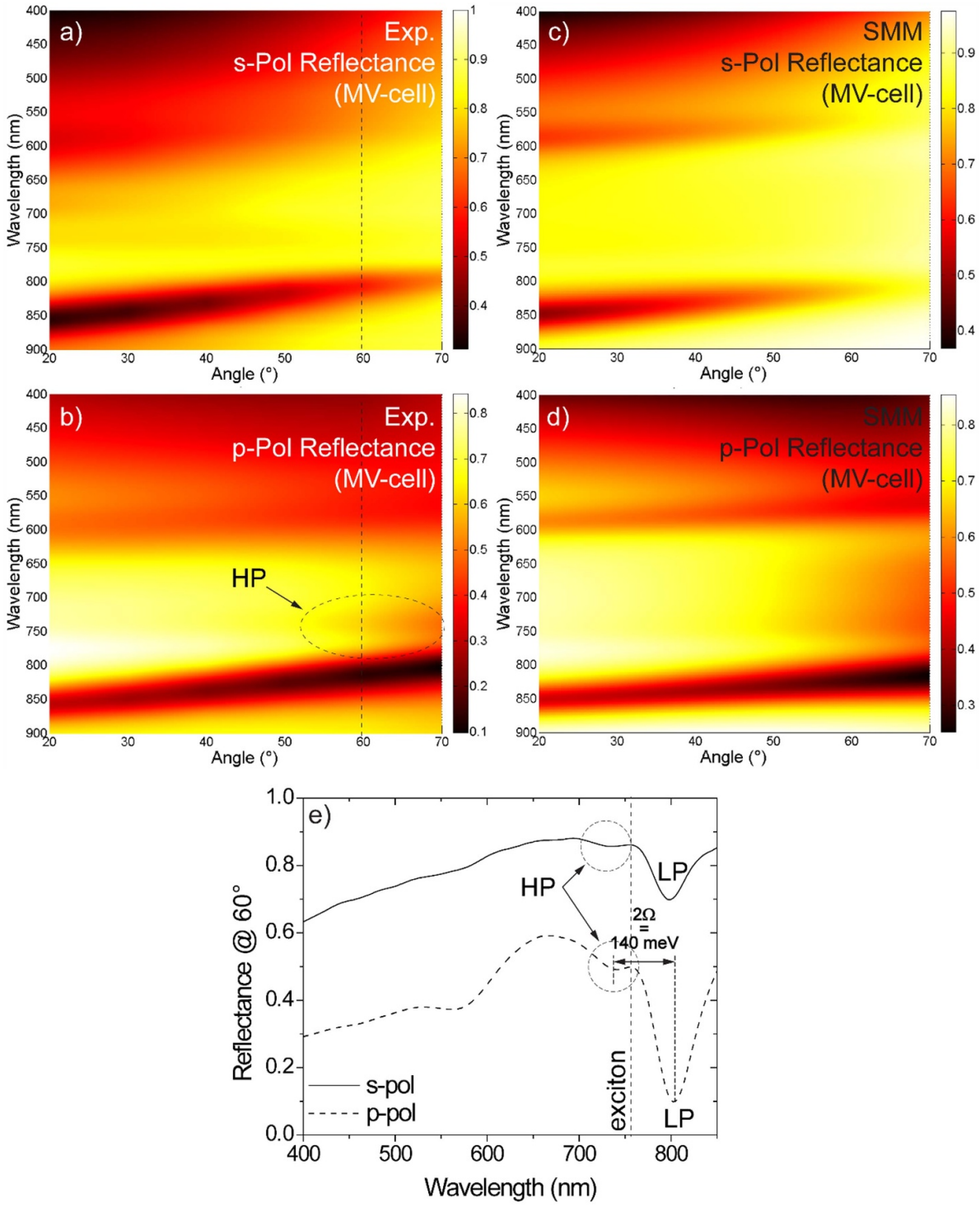

Figure 3. Experimental (a) s- and (b) p-polarization reflectance maps compared to the (c) s- and (d) p-polarization simulated ones for the MIM-cell as a function of the incidence angle. (e) P- and s-polarized reflectance spectra measured at $\theta = 60°$.

cavity configuration. Indeed, by recalling the aforementioned relation for the angular blue shift of the cavity mode it turns out that higher values of the real part of the effective refractive index related to the cavity dielectric core (n_{eff}) induce a smaller angular dispersion [20, 29, 30]. Exploiting the cavity angular dispersion constitutes also a wise way to sweep the cavity wavevector across the exciton of the active material to investigate the mode anti-crossing typical of the strong coupling regime without losing the optimized thickness of the active layer for the photovoltaic performances.

As we increase the incidence angle, the wavelength of the cavity mode moves towards the optical transition of the perovskite. At an incidence angle of $\sim 60°$, the resonant wavelength of the hypothetically unperturbed cavity would

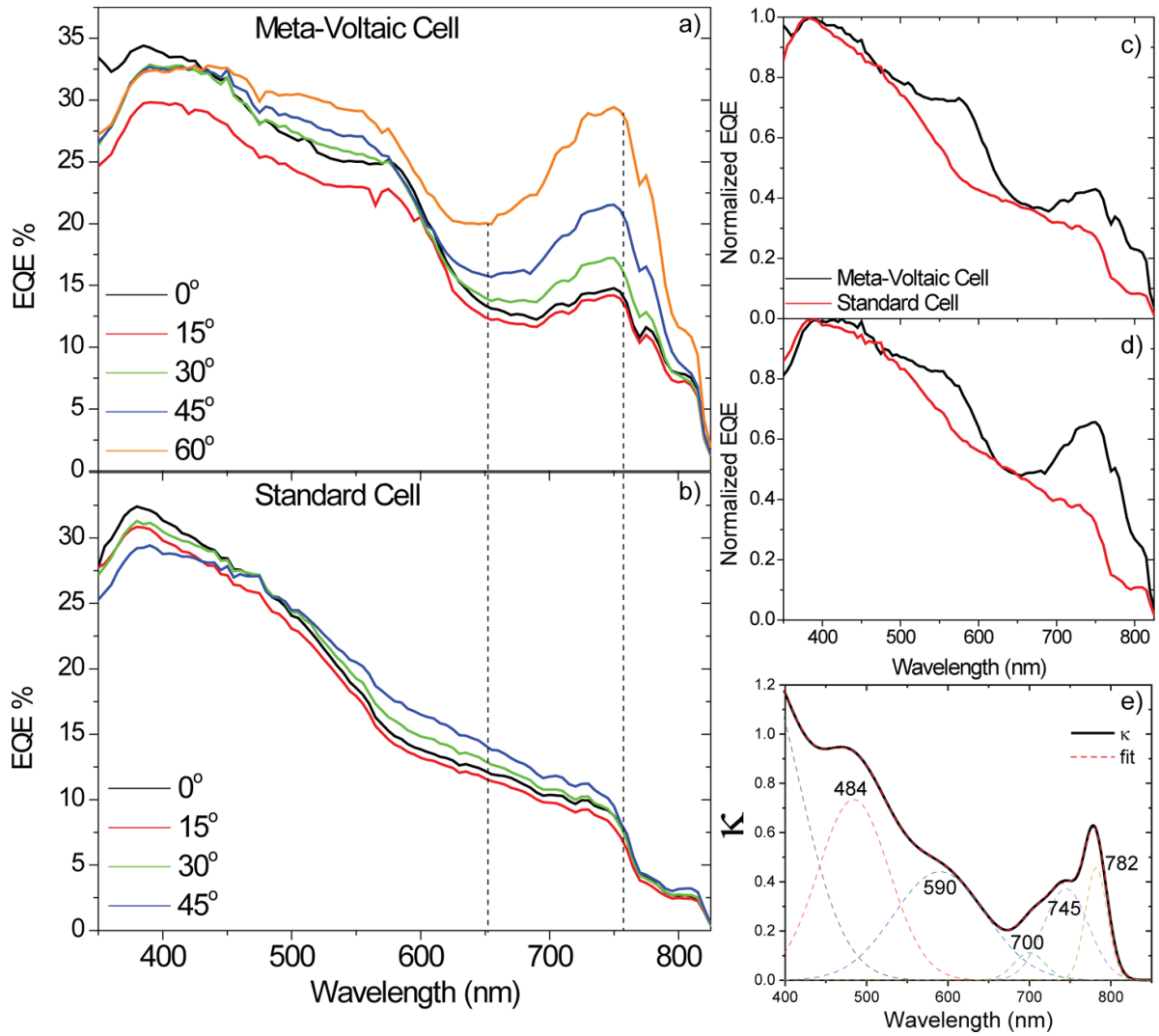

Figure 4. Angle-resolved EQE for (a) the MIM-cell and (b) a standard photovoltaic cell with analogous geometrical parameters, used as a benchmark. A direct comparison between the normalized EQE values of a standard cell and the corresponding MIM-cell is shown in (c) for normal incidence and (d) for 45° light incidence. The imaginary part of the refractive index of a pure film of perovskite is shown in (e), where a Gaussian fit of the ellipsometric angles allowed to identify four main Gaussian oscillators. The oscillator at 758 nm corresponds to lowest energy active optical transition of the perovskite, often referred to as 'the perovskite exciton' in this work.

reach the highest wavelength perovskite absorption. However, a modal splitting is observed, so that a pronounced dip in reflection is found for both p- and s-polarization at about 800 nm (figure 3(e)), and a second, less pronounced dip, is visible at about 730 nm. No reflectance dip is found at the exciton absorption wavelength, at about 758 nm (black curve of figure 3(e)). This is the signature of the occurrence of strong coupling between the cavity mode and the exciton. To confirm this aspect, we evaluated the Rabi splitting 2 Ω as the energy distance between HP and LP in the p-polarization curve and compared it with the energy linewidth of both the bare cavity mode and the excitonic transition of the perovskite. The energy linewidth of the bare cavity has been calculated by fitting with a Gaussian curve the reflectance dip occurring at about 850 nm in the p-polarization curve at an incidence angle of 30°, extrapolated from the reflectance map of figure 3(b), far from the strong coupling condition, to ensure that the mode holds a strong Fabry–Pérot character. The energy linewidth of the excitonic transition of the perovskite has been calculated directly from the imaginary part of its refractive index. The resulting values are: $2\Omega = 140$ meV, $\Delta E_{CAV} = 68$ meV and $\Delta E_{EXC} = 48$ meV. Since the condition $\Omega > \Delta E_{CAV} > \Delta E_{EXC}$ is verified, we can confirm the achievement of the strong coupling regime. We can, therefore, associate the former dip at 800 nm to the LP branch and the latter at 730 nm to the HP branch. Moreover, an additional dip in reflectance is detected at ∼575 nm, associated to a higher harmonic cavity mode.

To study how the photovoltaic properties of the MIM-cell are affected by the achievement of the strong coupling regime, angle-resolved EQE measurements were carried out and compared with the same measurements obtained on a benchmark standard photovoltaic cell, i.e. a cell in which the only difference is the absence of the bottom Au layer (see figure 1). Results are illustrated in figures 4(a)–(d).

A monotonic increase of EQE upon progressively slanting light illumination, from normal incidence ($\theta = 0°$, black curve) up to $\theta = 60°$ (orange curve) can be observed in figure 4(a) in the spectral region where polariton dispersion occurs, between 650 nm and 800 nm, where a doubling of the EQE values is recorded. In comparison, the EQE of a standard photovoltaic cell identical to the MIM-cell, but without the bottom Au layer, shows little dependence on light incidence angle, with just a slight EQE increase throughout most of the spectral range, as illustrated in figure 4(b). Given the relatively low light extinction achievable with a perovskite thickness of 180 nm, it seems reasonable to attribute this slight increase to the variation of the optical path when θ is increased.

However, in the MIM-cell an increase of EQE of similar entity was also detected in the 500–640 nm range, peaked around 570 nm. This is particularly evident if the normalized EQE values of the standard cell and of the MIM-cell at the same incidence angle are compared, as shown in figures 4(c) and (d) for two incidence angles. It is evident how the EQE increase observed in both the spectral areas centered at 570 nm and at 750 nm is present even for normal incidence. In addition, the high-wavelength EQE improvement becomes quantitatively more important for higher incidence angles.

The refractive index of a single perovskite film was measured by ellipsometry, in order to perform a comparison with the EQE behavior. The measurements, together with the associated Gaussian fit shown in section S6 of the supporting information, allowed us to identify the exact spectral position of the excitons (see figure 4(e)). Among them, the one centered at 782 nm corresponds to the lowest energy perovskite exciton, that can be associated to the direct band-gap transition. It is however true that, as can be evinced from figure 4(e), many other optical transitions are present in the absorption band of the perovskite, to each of which the formation of an exciton can be associated, as in the case for the ones peaked at 484 nm and 590 nm respectively, in figure 4(e). When the excitons related to these optical transitions are brought to interact with the high-energy cavity mode, strong coupling occurs as well. Therefore, the EQE enhancement occurring in the spectral region around 500–640 nm can be associated to the occurrence of polaritons as well. Even though the mechanism behind this effect has not been univocally clarified by theoretical studies, several possibilities were proposed. In fact, strong coupling was already investigated in photovoltaic systems based on organic materials, in which excitons are localized and their diffusion length is typically short. A reduced driving force for charge transfer, as well as a reduction of optical losses, were invoked by Nikolis *et al* to explain the improved EQE recorded in optical cavities [19]. Elsewhere the improved EQE recorded in optical cavities is attributed to an increased exciton diffusion length due to polaritons [12, 13]. Such a polariton-mediated excitation transport, allows a higher percentage of excitation to reach heterojunctions. If the charge transfer from polaritons at the heterojunction is fast enough to compete with polariton decay, the net effect is an improved energy harvesting.

In perovskites like the ones used in this work, excitons are typically more delocalized and their diffusion length much longer than in organics. Therefore, the effect of strong coupling could be expected to be mitigated in perovskite-based MIMs with respect to what observed in their organic counterparts. However, our results show that a relevant effect is also present when perovskites are used and only further studied can clarify whether this is due to similar or different mechanisms.

3. Conclusions

In conclusion, the experimental observations regarding both the photovoltaic effect and the scattering parameters indicate that two different and cooperating light–matter interaction regimes take place in the proposed system, consisting of a particular kind of photovoltaic cell in which the external electrodes constitute also the mirrors of a MIM resonant cavity. We called such a system 'MIM-cell'. In such a system, the strong-coupling between cavity modes and photo-generated excitons in the active material ($CH_3NH_3PbI_3$ perovskite) gives rise to cavity/exciton polaritons which determine an enhancement of the EQE of the MIM-cell of $\sim$100% in large areas of the absorption band. In particular, the enhancement of the EQE respects the angular polaritonic dispersion of the system so that, while increasing the angle of incidence of light radiation, the MIM-cell accesses the strong coupling regime, with a consequent gradual enhancement of EQE in the spectral ranges where the cavity acts as a resonator. Our findings, far from showcasing a new photovoltaic cell architecture, represent a remarkable example of coexisting and cooperating light–matter interaction regimes in a perovskite system, a condition to which a rich and partially unexplored phenomenology can be associated and possibly exploited. Since the strong coupling regime is as more effective as much Ω is larger than both ΔE_{CAV} and $\Delta E_{EXC,}$ it is reasonable to expect that minimizing these two quantities, for example by increasing the cavity Q-factor, could potentially increase the described performances.

4. Materials and methods

4.1. Chemicals

Poly(3,4-ethylenedioxythiophene) polystyrene sulfonate (PEDOT:PSS, Clevios PH 1000), methanamine hydriodide (MAI, 98%, 793493 Sigma Aldrich), lead iodide (PbI_2, 99.999, 900168 Sigma Aldrich), ammonium chloride (NH_4Cl, 99%, Carlo Erba), phenyl-C_{61}-butyric-acid-methyl-ester ([60]PCBM, 99.5%, Solenne BV), Bathocuproine (BCP, LT-E304 Lumtec), chlorobenzene (CB, anhydrous, 99.8%, 284513 Sigma Aldrich), isopropanol (IPA, anhydrous, 99.5%, 278475 Sigma Aldrich), toluene (anhydrous, 99.5%, 244511 Sigma Aldrich), N,N-Dimethylformamide anhydrous (DMF, anhydrous, 99.8%, 227056 Sigma Aldrich).

4.2. Solutions preparation

4.2.1. Perovskite $MAPbI_3$ precursor solution. Precursors MAI:PbI_2 (1:1) were dissolved in anhydrous DMF to obtain

a 0.6 M solution, stirred at 60 °C for 12 h in a nitrogen glovebox. When the solution reached room temperature, NH_4Cl was added with a molar ratio $MAI:PbI_2:NH_4Cl = 1:1:0.5$.

4.2.2. ETLs solutions. The PCBM solution was prepared by dissolving 20 mg of PCBM in 1 ml of anhydrous CB. The BCP solution was prepared by dissolving 0.5 mg of BCP in 1 ml of anhydrous IPA.

All solutions were filtered through a 0.22 μm pore PTFE filter and were stored in a glovebox.

4.3. Devices fabrication

4.3.1. Cell substrate. For the MIM-cell, a gold mirror layer of 80 nm was evaporated on the central part of a clean, indium-doped tin oxide (ITO)-coated glass, with a size of 15×25 mm^2. Then a thin layer of ITO was sputtered on the top of the gold layer. In the case of the standard photovoltaic cell, ITO-coated glass was used. The subsequent layer configuration was the same for both kinds of cells.

4.3.2. PEDOT:PSS layer deposition The PEDOT:PSS colloid was filtered by a 0.22 mm pore PVDF filter and spin coated at 3000 rpm for 60 s on the substrates, followed by annealing at 140 °C for 15 min in air.

4.3.3. $MAPbI_3$ layer. The perovskite active layer was deposited onto the above-prepared PEDOT:PSS layer by spin-coating at 5000 rpm for 60 s the precursor solution in a N_2 filled glovebox. Immediately after the spin-coating, the prepared film was heated at 100 °C for 30 s.

4.3.4. HTL layers. The [60] PCBM film was spin-coated onto the $MAPbI_3$ at 2000 rpm for 60 s. This was followed by the spin-coating of BCP at 6000 rpm for 20 s.

Finally, a very thin silver film, about 20 nm thick, was deposited by thermal evaporation in a high vacuum system (Kurt J Lesker) with a base pressure of 10^{-6} mbar.

4.4. Angle-resolved EQE

The light of a xenon lamp (300 W) was coupled into a monochromator (Newport 74100) and the resulting monochromatic light was focused onto the MIM or PV cell. The sample was mounted over a rotating holder and the EQE was measured at different angles. The current of the cell at short-circuit conditions was measured by using a source meter (Keithley 2400) between 350 nm and 850 nm, with steps of 5 nm. The EQE was determined by dividing the photocurrent density of the cell by the flux of incoming photons, which was obtained by using a calibrated silicon photodiode Hamamatsu mod. S2386-44 K.

4.5. Ellipsometry

The optical constants and thickness of each layer, as well as those of the MIM-cells, were obtained by spectroscopic ellipsometry, carried out by using an M2000 ellipsometer (Woollam). Reflectance (R) and transmittance (T) spectra were ellipsometrically measured. Such an approach gives precise results for multilayers of smooth films.

Data availability statement

All data that support the findings of this study are included within the article (and any supplementary files).

Acknowledgments

The present work was partially financed by 'Progetto STAR 2—PIR01_00008'—Ministero dell'Università e Ricerca/Italian Ministry of University and Research.

V C thanks the research project 'Componenti Optoelettronici Biodegradabili ed Eco-Sostenibili verso la nano-fotonica "green"' (D.M. n. 1062, 10.08.2021, PON 'Ricerca e Innovazione' 2014-2020), contract identification code 1062_R17_GREEN.

G E L thanks the research project 'FSE-REACT EU' financed by National Social Fund—National Operative Research Program and Innovation 2014-2020 (D.M. 1062/2021) contract identification code 10-G-15049-2.

ORCID iDs

V Caligiuri https://orcid.org/0000-0003-1035-4702
S Siprova https://orcid.org/0000-0003-2901-8805
A De Luca https://orcid.org/0000-0003-2428-9075

References

[1] Scully M O and Zubairy M S 1997 *Quantum Optics* (Cambridge University Press)
[2] Haroche S and Kleppner D 1989 Quantum cavity electrodynamics *Phys. Today* **42** 24–30
[3] Sanvitto D and Kéna-Cohen S 2016 The road towards polaritonic devices *Nat. Mater.* **15** 1061–73
[4] Savasta S, Saija R, Ridolfo A, Di Stefano O, Denti P and Borghese F 2010 Nanopolaritons: vacuum Rabi splitting with a single quantum dot in the center of a dimer nanoantenna *ACS Nano* **4** 6369–76
[5] Chen S, Liu J, Lu H, Wang Q and Zhu Y 2012 Strong coupling effects between a meta-atom and MIM nanocavity *AIP Adv.* **2** 032186
[6] Frisk Kockum A, Miranowicz A, De Liberato S, Savasta S and Nori F 2019 Ultrastrong coupling between light and matter *Nat. Rev. Phys.* **1** 19–40
[7] Patra A, Caligiuri V, Krahne R and Luca A D 2021 Strong light–matter interaction and spontaneous emission reshaping via pseudo-cavity modes *Adv. Opt. Mater.* **9** 2101076
[8] Kang E S, Chen S, Đerek V, Hägglund C, Głowacki E D and Jonsson M P 2021 Charge transport in phthalocyanine thin-film transistors coupled with Fabry–Perot cavities *J. Mater. Chem.* C **9** 2368–74
[9] Yu M-W, Ishii S, Li S, Ku J-R, Yang J-H, Su K-L, Taniguchi T, Nagao T and Chen K-P 2021 Quantifying photoinduced carriers transport in exciton–polariton coupling of MoS_2 monolayers *npj 2D Mater. Appl.* **5** 1–7

[10] Xiang B, Ribeiro R F, Li Y, Dunkelberger A D, Simpkins B B, Yuen-Zhou J and Xiong W 2019 Manipulating optical nonlinearities of molecular polaritons by delocalization *Sci. Adv.* **5** eaax5196
[11] Feist J and Garcia-Vidal F J 2015 Extraordinary exciton conductance induced by strong coupling *Phys. Rev. Lett.* **114** 196402
[12] DelPo C A, Khan S-U-Z, Park K H, Kudisch B, Rand B P and Scholes G D 2021 Polariton decay in donor–acceptor cavity systems *J. Phys. Chem. Lett.* **12** 9774–82
[13] Wang M, Hertzog M and Börjesson K 2021 Polariton-assisted excitation energy channeling in organic heterojunctions *Nat. Commun.* **12** 1874
[14] Zeb M A, Kirton P G and Keeling J 2020 Incoherent charge transport in an organic polariton condensate (arXiv:2004.09790)
[15] Liu B, Huang X, Hou S, Fan D and Forrest S R 2022 Photocurrent generation following long-range propagation of organic exciton–polaritons *Optica* **9** 1029–36
[16] Chervy T, Knüppel P, Abbaspour H, Lupatini M, Fält S, Wegscheider W, Kroner M and Imamoğlu A 2020 Accelerating polaritons with external electric and magnetic fields *Phys. Rev.* X **10** 011040
[17] Schachenmayer J, Genes C, Tignone E and Pupillo G 2015 Cavity-enhanced transport of excitons *Phys. Rev. Lett.* **114** 196403
[18] Lerario G *et al* 2017 High-speed flow of interacting organic polaritons *Light: Sci. Appl.* **6** e16212
[19] Nikolis V C *et al* 2019 Strong light-matter coupling for reduced photon energy losses in organic photovoltaics *Nat. Commun.* **10** 3706
[20] Caligiuri V, Palei M, Biffi G, Artyukhin S and Krahne R 2019 A semi-classical view on epsilon-near-zero resonant tunneling modes in metal/insulator/metal nanocavities *Nano Lett.* **19** 3151–60
[21] Akkerman Q A, Gandini M, Di Stasio F, Rastogi P, Palazon F, Bertoni G, Ball J M, Prato M, Petrozza A and Manna L 2016 Strongly emissive perovskite nanocrystal inks for high-voltage solar cells *Nat. Energy* **2** 1–7
[22] Cacciola A, Di Stefano O, Stassi R, Saija R and Savasta S 2014 Ultrastrong coupling of plasmons and excitons in a nanoshell *ACS Nano* **8** 11483–92
[23] Patra A, Caligiuri V, Zappone B, Krahne R and De Luca A 2023 In-plane and out-of-plane investigation of resonant tunneling polaritons in metal–dielectric–metal cavities *Nano Lett.* **23** 1489–95
[24] Qing Y M, Ma H F and Cui T J 2019 Theoretical analysis of tunable multimode coupling in a grating-assisted double-layer graphene plasmonic system *ACS Photonics* **6** 2884–93
[25] Qing Y M, Ma H F and Cui T J 2020 Strong coupling between excitons and guided modes in WS_2-based nanostructures *J. Opt. Soc. Am.* B **37** 1447–52
[26] Wu J and Qing Y M 2022 Strong coupling of exciton and guided mode in perovskite film with high fabrication-tolerant scheme *Opt. Laser Technol.* **155** 108437
[27] Qing Y M, Ma H F and Cui T J 2019 Investigation of strong multimode interaction in a graphene-based hybrid coupled plasmonic system *Carbon* **145** 596–602
[28] Qing Y M, Ren Y, Lei D, Ma H F and Cui T J 2022 Strong coupling in two-dimensional materials-based nanostructures: a review *J. Opt.* **24** 024009
[29] Caligiuri V, Biffi G, Palei M, Martín-García B, Pothuraju R D, Bretonnière Y and Krahne R 2019 Angle and polarization selective spontaneous emission in dye-doped metal/insulator/metal nanocavities *Adv. Opt. Mater.* **8** 1901215
[30] Caligiuri V, Palei M, Biffi G and Krahne R 2019 Hybridization of epsilon-near-zero modes via resonant tunneling in layered metal-insulator double nanocavities *Nanophotonics* **8** 1–8